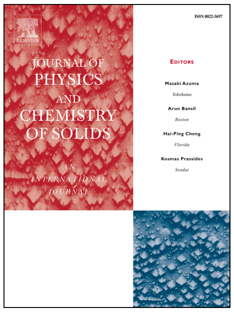

Comparative study on the effect of adding two transition-metal-substituted polyoxometalates on the mechanical properties of the (Bi,Pb)-2223 superconducting phase

Nour El Ghouch, Rami Al-Oweini, Khulud Habanjar, R. Awad

PII: S0022-3697(20)31443-8

DOI: https://doi.org/10.1016/j.jpcs.2020.109807

Reference: PCS 109807

To appear in: *Journal of Physics and Chemistry of Solids*

Received Date: 28 May 2020

Revised Date: 12 October 2020

Accepted Date: 13 October 2020

Please cite this article as: N. El Ghouch, R. Al-Oweini, K. Habanjar, R. Awad, Comparative study on the effect of adding two transition-metal-substituted polyoxometalates on the mechanical properties of the (Bi,Pb)-2223 superconducting phase, *Journal of Physics and Chemistry of Solids* (2021), doi: https://doi.org/10.1016/j.jpcs.2020.109807.

CRediT author statement

Nour El Ghouch: Software, Validation, Formal analysis, Investigation, Data Curation, Writing - Original Draft, Visualization
Rami Al-Oweini: Conceptualization, Writing - Review & Editing, Project administration
Khulud Habanjar: Supervision
R Awad: Conceptualization, Methodology, Project administration

Comparative study on the effect of adding two transition-metal-substituted polyoxometalates on the mechanical properties of the (Bi,Pb)-2223 superconducting phase

Nour El Ghouch[a], Rami Al-Oweini[a,†,*], Khulud Habanjar[b], R Awad[b,*]

[a]Department of Chemistry, Faculty of Science, Beirut Arab University, P.O. Box 11-5020 Riad El Solh, Beirut, Lebanon
[b]Department of Physics, Faculty of Science, Beirut Arab University, P.O. Box 11-5020 Riad El Solh, Beirut, Lebanon
[†]Present address: Kamal A. Shair Central Research Science Laboratory, Faculty of Arts and Sciences, American University of Beirut, P.O. Box: 11-0236, Riad El-Solh 1107 2020, Beirut, Lebanon

Rami Al-Oweini
Department of Chemistry
Faculty of Science; Beirut Arab University
P.O. Box 11-5020 Riad El Solh, Beirut, Lebanon
Phone: +961 7 985881 Ext 3316
Email: roweini@gmail.com

R Awad
Department of Physics
Faculty of Science; Beirut Arab University
P.O. Box 11-5020 Riad El Solh, Beirut, Lebanon
Phone: +961 7 985881 Ext 3300
Email: ramadan.awad@bau.edu.lb

Abstract

This comparative study sheds light on the optimum addition *x* of $K_5[SiFe(OH_2)W_{11}O_{39}]\cdot 14H_2O$ ({$FeSiW_{11}$}) and $K_6[(H_2O)MnSiW_{11}O_{39}]\cdot 21H_2O$ ({$MnSiW_{11}$}) (x = 0.02, 0.04, 0.08, 0.12, 0.16 and 0.20 wt.%) nanoparticles to produce the desired mechanical characteristics of the (Bi,Pb)-2223 superconducting phase using a Vickers microhardness (H_V) tester. H_V measurement was performed at room temperature for different applied loads (0.245–9.8 N) and times (10–60 s). From the H_V measurements, all the prepared samples had a normal 'indentation size effect' behaviour. It was found that 0.04 wt.% {$FeSiW_{11}$} nanoparticles and 0.08 wt.% {$MnSiW_{11}$} nanoparticles were the optimal addition to increase the microhardness of the (Bi,Pb)-2223 phase. Accordingly, other mechanical parameters for potential applications, such as the elastic modulus, yield strength and fracture toughness of the samples studied, were extracted from H_V as a function of nanoparticle addition. The measured H_V data were theoretically analysed with use of different models. The modified proportional sample resistance model was identified as the best theoretical model to describe the true H_V values for both phases. Indentation creep analysis was also performed using time-dependent microhardness to indicate the enhancement of new cavity formation in the measured samples.

Keywords: Polyoxometalates; (Bi,Pb)-2223 superconductor; Vickers microhardness; Creep indentation

1. Introduction

Among high-temperature superconductors, the $(Bi_{1.8}Pb_{0.4})Ca_2Sr_2Cu_3O_{10+\delta}$ (Bi,Pb)-2223 phase appears to be an interesting candidate for technological and industrial applications [1]. It is characterized by a high transition temperature (T_c) and critical current density (J_c) [2], as well as a needle-like or flake-like structure. Unfortunately, however, the structure of the (Bi,Pb)-2223 phase has several serious drawbacks that limit the use of this material for the fabrication of wires and tapes [3]. For example, the porous structure, brittleness, low ductility and toughness [4, 5] decrease J_c and the upper critical field when a mechanical stress is applied. Generally, the internal structure of any material specifies its mechanical properties, such as Vickers microhardness, Young's modulus and yield strength. To improve these properties, structural modifications should be made. Consequently, in recent decades, one of the most effective and practical approaches is the use of pores between the grains in the structure by the addition/substitution of nanoparticles in superconductor composites [1, 2, 4, 6–13].

There are many techniques to estimate the microhardness and mechanical properties of ceramic materials; however, the most familiar and preferable method is the Vickers microhardness (H_V) technique [1, 14]. Among the various scales, this method is quick, efficient, simple, accurate and mainly non-destructive [15, 16]. Additionally, it supplies structural parameters, such as strength and deformation properties [15]. Thus, hardness tests are useful in characterizing materials for practical applications [8]. The mechanical characteristics of high-temperature superconductors have been investigated for several years [17–22], including microparticle substitution, nano-oxides, nanometals and nanomagnetic materials. For instance, the effect of holmium nanoparticles on the (Bi,Pb)-2223 superconducting phase was studied by Abdeen et al. [2], where a low amount of holmium ($x = 0.025$ wt.%) improved the mechanical properties of the (Bi,Pb)-2223 superconducting phase. On the other hand, Özkurt [23] demonstrated the effect of addition of WO_3 (40 nm) on the $Bi_{1.8}Sr_2W_xCa_{1.1}Cu_{2.1}O_y$ superconductor, revealing that a high added concentration of WO_3 ($x = 0.25$ wt.%) increased the microhardness of the phase. Additionally, Cevizci et al. [4] reported that the substitution of 0.12 wt.% Ag increased the microhardness of the (Bi,Pb)-2223 phase, and a normal indentation size effect (ISE) behaviour was obtained. Habanjar et al. [11] found that the addition of up to 0.75 wt.% magnetic nanosized $BaFe_{12}O_{19}$ to the (Bi,Pb)-2223 superconductor had a significant effect as demonstrated by the increased microhardness of this phase.

On the other hand, polyoxometalates (POMs), which are considered a family of molecular and nanosized metal–oxygen assemblies, are an interesting class of inorganic nanomaterials with a wide structural variety and special properties [24–26]. They have potential applications in diverse areas such as catalysis, nanotechnology and materials science [27–31].

In our previous work we found that the POMs $K_5[SiFe(OH_2)W_{11}O_{39}]\cdot 14H_2O$ ($\{FeSiW_{11}\}$) and $K_6[(H_2O)MnSiW_{11}O_{39}]\cdot 21H_2O$ ($\{MnSiW_{11}\}$) are very useful for enhancing the electrical and the dielectric properties, respectively, of the (Bi,Pb)-2223 superconductor [32, 33]. X-ray diffraction analysis showed that the addition of small amounts of $\{FeSiW_{11}\}$ or $\{MnSiW_{11}\}$ nanoparticles improves the (Bi,Pb)-2223 phase formation significantly. Besides, the superconducting transition temperature (T_c) was enhanced with increase of the amount of $\{MnSiW_{11}\}$ and $\{FeSiW_{11}\}$ up to 0.12 and 0.16 wt.%, respectively. The transport critical current density (J_c) was increased with up to 0.12 wt.% $\{MnSiW_{11}\}$ or $\{FeSiW_{11}\}$, after which T_c and J_c were reduced with further increase in x. Furthermore, dielectric measurements showed that the $\{MnSiW_{11}\}$ addition resulted in a greater increase than $\{FeSiW_{11}\}$ addition, specifically for $x = 0.12$ wt.% [34].

To the best of our knowledge, no study has previously been reported on H_V testing and the mechanical properties of iron- and manganese-containing POM nanoparticles ($\{FeSiW_{11}\}$ and $\{MnSiW_{11}\}$, respectively) added to the (Bi,Pb)-2223 superconducting phase. In this work, a comparative study between the two POMs was conducted to identify the more desirable material for enhancing the mechanical properties of the (Bi,Pb)-2223 superconducting phase. Additionally, the load-dependent and load-independent microhardness of the $\{FeSiW_{11}\}_x$(Bi,Pb)-2223 and $\{MnSiW_{11}\}_x$(Bi,Pb)-2223 superconducting samples ($0.00\ wt.\% \leq x \leq 0.20\ \mathrm{wt.\%}$) were assessed with an H_V tester. The prepared samples were characterized by Brunauer–Emmett–Teller (BET) measurements. Moreover, the true microhardness parameters in the saturation limit regions of the samples without and with addition of either type of nanoparticles were characterized by various empirical and theoretical models. Furthermore, the indentation creep mechanism for the prepared samples was determined from the time-dependent microhardness results.

2. Experimental procedure

The POMs $\{FeSiW_{11}\}$ and $\{MnSiW_{11}\}$ and the superconducting samples were synthesized by the solid-state reaction method as reported in our previous work [32, 33, 35].

2.1. Characterization of superconducting samples

The surface area, pore size and pore volume, as well as the distribution of the POMs on the (Bi,Pb)-2223 superconducting phase, were determined with a NOVA 2200 automated BET surface area analyser. To study the mechanical performance of the prepared superconducting samples, the H_V values were measured with a digital microhardness tester (MHVD-1000IS) at room temperature. Throughout the measurements, the applied static loads were 0.245–9.8 N with different loading times from 10 to 60 s. By use of a calibrated microscope, the diagonals of the indentation were determined; thus, the load-dependent microhardness was calculated with the relationship

$$H_V = \frac{2F\sin(\frac{\alpha}{2})}{d^2} = 1854.4 \times \frac{F}{d^2}\ (\mathrm{GPa}), \qquad (1)$$

where F is the applied static load in newtons, α is the face angle of 136° for the indenter and d is the diagonal length of the indentation in micrometres. The indentation process was performed five times at different sites on the surface of the examined specimens to calculate the mean value of H_V for each load. Additionally, the mechanical properties dependent on the microhardness were calculated, such as the elastic modulus (E), the yield strength (Y) and the fracture toughness (K), according to the following equations:

$$E = 81.9635\, H_{\mathrm{V}}, \tag{2}$$

$$Y = \frac{H_{\mathrm{V}}}{\mathbf{3}}, \tag{3}$$

$$K = \sqrt{2E\alpha}. \tag{4}$$

They are defined as follows: E is the tendency of the material to be deformed elastically under an applied force; Y is denoted as the transition point from elastic deformation to plastic deformation; K is one of the most important features in selecting materials for industrial applications because it describes the capability of the material to resist cracks, propagation and fracture. Because the H_{V} measurements were performed at various times, indentation creep tests were performed to illustrate the behaviour of the indentation creep at a fixed applied load for $\{\mathrm{FeSiW_{11}}\}$ and $\{\mathrm{MnSiW_{11}}\}$ nanoparticles added to the (Bi,Pb)-2223 phase.

3. Results and discussion

3.1. Sample characterization

Figs. 1 and 2 show the typical N_2 adsorption–desorption isotherm and Brunauer–Joyner–Halenda pore size distribution plots for $\{\mathrm{FeSiW_{11}}\}_x$(Bi,Pb)-2223 and $\{\mathrm{MnSiW_{11}}\}_x$(Bi,Pb)-2223 superconducting samples with $x = 0.00$, 0.04, 0.08 and 0.12 wt.%. Type II adsorption isotherms are seen in Fig. 1, with negligible hysteresis loops [36]. The open loops of such adsorption isotherms are reported to manifest the existence of non-rigid aggregates in the presence of a network of macropores [36]. In a similar fashion, in different research into other hybrid aggregate materials, similar results showing an open loop were obtained [37]. By the BET method, the specific surface area (SSA) of the superconducting samples was calculated according to Eq. (5) and the values obtained are presented in Table 1 [38]:

$$S_{\mathrm{BET}} = \frac{a\, P_0\, V_{\mathrm{m}}\, N_{\mathrm{A}}}{273R}, \tag{5}$$

where that a is the N_2 molecule's area, P_0 is the adsorbate's saturation pressure at the adsorption temperature, V_{m} is the adsorbed gas volume and R is the gas constant. Moreover, the Brunauer–Joyner–Halenda method was used to calculate the pore size distribution according to the following formula, as shown in Fig. 2 and presented in Table 1 [39]:

$$V_{\mathrm{p}n} = \frac{r_{\mathrm{p}n}^2}{(r_{\mathrm{k}n} + \Delta t_n)^2}\Delta V_n - \frac{r_{\mathrm{p}n}^2}{(r_{\mathrm{k}n} + \Delta t_n)^2}\Delta t_n \sum_{j=1}^{n-1} \frac{r_{\mathrm{p}j} - t_j}{r_{\mathrm{p}j}} A_{\mathrm{p}j}, \tag{6}$$

where $r_{\mathrm{p}n}$ is the pore size, $r_{\mathrm{k}n}$ is the inner capillary radius, Δt_n is the layer thickness change and ΔV_n is the volume desorbed in each desorption step, respectively, and $A_{\mathrm{p}} = 2\frac{V_{\mathrm{p}}}{r_{\mathrm{p}}}$. It is clear from Table 1 that the SSA of the pure sample ($x = 0.00\,\mathrm{wt.\%}$) was 0.56 $\mathrm{m^2/g}$. However, by our introducing the POM {$\mathrm{FeSiW_{11}}$} up to 0.04 wt.% on the superconducting material surface, a significant increase in the SSA from 0.56 to 14.48 $\mathrm{m^2/g}$ was observed, indicating the successful dispersion of the nanoparticles on the superconducting phase. On the other hand, high additions of {$\mathrm{FeSiW_{11}}$} ($x = 0.08\,\mathrm{wt.\%}$) and {$\mathrm{MnSiW_{11}}$} ($x = 0.12\,\mathrm{wt.\%}$) resulted in a decrease in the SSA to 9.69 and 0.42 $\mathrm{m^2/g}$, respectively. This is attributed to the increased accumulation of the nanoparticles at the (Bi,Pb)-2223 superconducting phase grain boundary [40].

3.2. Vickers microhardness measurements

To examine the effect of the addition of {$\mathrm{FeSiW_{11}}$} and {$\mathrm{MnSiW_{11}}$} nanoparticles ($0.00\,\mathrm{wt.\%} \leq x \leq 0.20\,\mathrm{wt.\%}$) on the mechanical properties of (Bi,Pb)-2223 superconducting samples, several microhardness measurements were performed on the surface of the prepared samples at room temperature. The H_{V} values were determined with Eq. (1). The measured H_{V} values versus the applied static test load F at a dwell time of 30 s for {$\mathrm{FeSiW_{11}}$}$_x$(Bi,Pb)-2223 and {$\mathrm{MnSiW_{11}}$}$_x$(Bi,Pb)-2223 with x = 0.00, 0.04, 0.08, 0.12 and 0.20 wt.% are shown graphically in Fig. 3. It is clearly shown that the experimental H_{V} curves exhibit a non-linear decrease in the original microhardness for an applied load up to 2.94 N. After this critical load, the H_{V} values reach a saturation limit (plateau region) and the applied load has no significant effect on the microhardness values. This behaviour is well known as a normal ISE, and it is related to the weak grain boundaries of ceramic materials. It was explained by Foerster et al. [41] and Sahoo et al. [42] with respect to the penetration depth of the indenter. The surface layers are affected by the application of small loads only, whereas for higher loads, the penetration is increased and the effect of the inner layers becomes more integral.

On the other hand, the H_{V} values for {$\mathrm{FeSiW_{11}}$}$_x$(Bi,Pb)-2223 phase samples were observed to be within 1.125–2.125 GPa for a static load of 0.245 N and within 0.75–0.9 GPa for a static load of 9.8 N. However, for the {$\mathrm{MnSiW_{11}}$}$_x$(Bi,Pb)-2223 phase, the H_{V} values obtained were 0.7–1.125 GPa for a static load of 0.245 N and 0.5–0.75 GPa for a static load of 9.8 N. It is obvious that {$\mathrm{FeSiW_{11}}$} nanoparticles have a greater microhardness parameter enhancement effect on the (Bi,Pb)-2223 phase than {$MnSiW_{11}$} nanoparticles. In other words, H_V increased as the addition of {$FeSiW_{11}$} and {$MnSiW_{11}$} increased up to $0.04\ \mathrm{wt.\%}$ for {$FeSiW_{11}$}$_x$(Bi,Pb)-2223 and up to $0.08\ \mathrm{wt.\%}$ for {$MnSiW_{11}$}$_x$(Bi,Pb)-2223. H_V decreased for both phases as x increased up to $0.20\ \mathrm{wt.\%}$. Therefore, {$FeSiW_{11}$} and {$MnSiW_{11}$} both have a significant effect in increasing the microhardness of the (Bi,Pb)-2223 phase. The enhancement is attributed to an improvement in the grain connectivity [22] resulting from the lower values of porosity as shown in Fig. 12, and resistance to crack propagation between the grains [2, 22]. In addition, this fact can be explained by the increase in the SSA obtained from the BET analysis, indicating the successful distribution of the POMs at a low concentration on the material surface. By contrast, the reduction of H_V for both {$FeSiW_{11}$}$_x$(Bi,Pb)-2223 with $x \geq 0.04\ \mathrm{wt.\%}$ and {$MnSiW_{11}$}$_x$(Bi,Pb)-2223 with $x \geq 0.08\ \mathrm{wt.\%}$ was attributed to the increase in the porosity, disorders and grain boundary weak links, in addition to the formation of impurity phases with an irregular grain orientation distribution that led to a change in the bond length [3, 18], as well as the decrease in the SSA identified from the BET measurements. Therefore, Table 2 shows that the addition of 0.04 wt.% {$FeSiW_{11}$} enhanced the load-independent H_V by 173.88%, whereas addition of 0.08 wt.% {$MnSiW_{11}$} enhanced H_V by 103.35%. Moreover, when comparing the H_V values obtained in our work with prior literature results [2, 4, 23], one can see that the increase obtained is greater than that reported previously. It was also found that the addition of Ho, WO_3 and Ag to the (Bi,Pb)-2223 superconductor increased H_V by 4.74%, 54.6% and 9.75%, respectively. On the other hand, the addition of magnetic nanosized $BaFe_{12}O_{19}$ by Habanjar et al. [11] resulted in a greater increase in H_V compared with the present study, with an increase of 250.2%. This indicates that the {$FeSiW_{11}$} POM is better for enhancing the mechanical properties of the (Bi,Pb)-2223 superconductor. It is interesting to note that the {$FeSiW_{11}$} POM was also found to better at increasing T_c, although the volume fraction was increased more by the {$MnSiW_{11}$} POM.

Furthermore, the fitting equations describing the variation of H_V with the applied load according to the quadratic formulas for all samples are presented in Table 2. The variation of the x^2 coefficients increased regularly from 0.0073 to 0.0332 as the added concentration of {$FeSiW_{11}$} increased to $0.04\ \mathrm{wt.\%}$ and increased from 0.0073 to 0.0269 for {$MnSiW_{11}$} addition. This finding is attributed to the decrease in the number of cracks and dislocations throughout the Cu–O_2 stacked layers, which is related to the increase of hardness [1]. Additionally, the variation of x^2 decreased with further increases in x up to 0.20 wt.%, likely due to the rapid increase of the omnipresent flaws in the crystal structure and the number of dislocations in the superconducting layers, along with the enhancement of impurity phases resulting from relative volume fractions [1, 14].

To assess the change of H_V with the applied static load F in the plateau limit regions, namely the true microhardness or load-independent microhardness, several theoretical models were applied. This allowed us to achieve the mechanical characterization of the $\{FeSiW_{11}\}_x$(Bi,Pb)-2223 and $\{MnSiW_{11}\}_x$(Bi,Pb)-2223 superconducting samples. In this study, Meyer's law, the Hays–Kendall (HK) model, the elastic–plastic deformation (EPD) model, the proportional sample resistance (PSR) model and the modified PSR (MPSR) model were used to investigate our measured results.

3.2.1. Meyer's law

Meyer's law is a popular theoretical law to define the normal ISE or reverse ISE (RISE) behaviour of materials. It relates the static applied load and diagonal length of the indentation:

$$F = Ad^n, \qquad (7)$$

where A is the typical microhardness constant and n is Meyer's number, which is a measure of ISE or RISE. For $n < 2$, H_V decreases with an increase in the applied load, and a typical normal ISE behaviour will be observed. For $n > 2$, RISE behaviour is observed (in contrast to an ISE behaviour). However, if $n = 2$, the microhardness is independent of the applied static load (Kick's law) [16]. Hence, to determine the behaviour of the prepared superconducting samples, $\ln F$ versus $\ln d$ for $\{FeSiW_{11}\}_x$(Bi,Pb)-2223 and $\{MnSiW_{11}\}_x$(Bi,Pb)-2223 with x = 0.00, 0.04, 0.08, 0.12 and 0.20 wt.% was plotted, and is presented in Fig. 4. Meyer's number is obtained from the slope of the linear plot and A is obtained from the intercept; their values are summarized in Table 3. Accordingly, the n values are less than 2 in both phases for all the superconducting samples, verifying normal ISE behaviour. Similar behaviour was obtained by Cevizci et al. [4] in the (Bi,Pb)-2223 superconducting phase. Furthermore, n can be used to classify the hardness of the materials: if n is between 1 and 1.6, the material is hard; if n is greater than 1.6, the material is soft [7, 9]. As seen from Table 3, all the prepared samples are classified as hard materials, confirming the ceramic behaviour of high-temperature superconductors.

3.2.2. Hays–Kendall model

This model suggests that under a minimum applied load W only the character of the plastic deformation predominates [14, 43]. This means that the indenter can more easily spike the superconducting samples for a higher indentation load. Accordingly, the variation of the effective load with the indentation impression length is given by the following formula:

$$\boldsymbol{F = A_1 d^2 + W}, \qquad (8)$$

where A_1 is the load-independent microhardness constant and W is the practical indentation test load. Fig. 5 shows the linear fitting of F versus d^2 for the $\{FeSiW_{11}\}_x$(Bi,Pb)-2223 and $\{MnSiW_{11}\}_x$(Bi,Pb)-2223 samples, from which A_1 and W were obtained and are listed in Table 3. The W values are positive in both phases (demonstrating typical ISE behaviour), indicating that the applied static load is adequate to create both elastic and plastic deformation [2]. However, the decrease in A_1, especially at high added concentrations of $\{FeSiW_{11}\}$ and $\{MnSiW_{11}\}$ nanoparticles, may be explained as due to the increase in the microstructure disorders and boundary weak links between the superconducting grains of the (Bi,Pb)-2223 phase [14]. The load-independent microhardness (H_{HK}) was determined in the plateau region with use of the following equation (the values are presented in Table 2):

$$H_{\mathrm{HK}} = 1854.4 \times A_1. \qquad (9)$$

According to the H_V theoretical data summarized in Table 2, much lower values of H_{HK} were found than the experimental microhardness values in the plateau region. Accordingly, the HK model is inappropriate to examine the behaviour of true microhardness in both phases.

3.2.3. Elastic–plastic deformation model

The EPD model states that the indentation impression involves a small elastic deformation that tends to recover on the removal of an applied static load [44, 45]. Consequently, a new extra term for elastic deformation (d_0) was added to the indentation diagonal length d, corresponding to plastic deformation, as given in the following equation:

$$F = A_2 (d + d_0)^2, \qquad (10)$$

where A_2 is the real microhardness constant, from which the corresponding load-independent elastic–plastic microhardness (H_{EPD}) was calculated according to the following equation (the values are listed in Table 2):

$$H_{\mathrm{EPD}} = 1854.4 \times A_2. \qquad (11)$$

The linear plot of $F^{0.5}$ versus d for the $\{FeSiW_{11}\}_x$(Bi,Pb)-2223 and $\{MnSiW_{11}\}_x$(Bi,Pb)-2223 superconducting samples is presented in Fig. 6. A_2 and d_0 were determined and are summarized in Table 3. Accordingly, the d_0 values were positive in both phases for all of the samples. This means that elastic deformation along with plastic deformation was observed in the presence of elastic relaxation for all the prepared samples [18], explaining their ISE behaviour. The reduction in A_2 for $x \geq 0.04\ \mathrm{wt.\%}$ is attributed to the increase in the local structural disorders and boundary weak links between the superconducting grains, leading to a decrease in the measured microhardness and crack propagation [14]. It is evident from Table 2 that the H_{EPD} values are far from the original microhardness values in the plateau region; thus, this model is unsuitable to discuss our experimental data.

3.2.4. Proportional sample resistance model

This model can be used to define the ISE behaviour according to the following equation [46]:

$$F = \alpha d + \beta d^2, \qquad (12)$$

where α denotes the surface energy and β is the true microhardness coefficient, which was used to calculate the true PSR microhardness (H_{PSR}) with use of Eq. (13) [18]:

$$H_{PSR} = 1854.4 \times \beta. \qquad (13)$$

Li and Bradt [46] suggested that α and β are related to both the elastic properties and the plastic properties of materials. Moreover, they proposed that α comprises two components: the elastic resistance of the test specimen and friction resistance assessed by the indenter.

Fig. 7 shows plots of F/d against d for $\{FeSiW_{11}\}_x$(Bi,Pb)-2223 and $\{MnSiW_{11}\}_x$(Bi,Pb)-2223 superconducting samples; thus, α and β were calculated, and are shown in Table 3. The curves clearly represent an excellent linear relationship. It is obvious from Table 3 that the positive values of α confirm the existence of elastic deformation as well as plastic deformation, showing ISE behaviour in the specimens studied [19]. These findings are also consistent with the HK approach. Furthermore, the α values in both phases were increased by our increasing the content of $\{FeSiW_{11}\}$ and $\{MnSiW_{11}\}$ nanoparticles for samples with $x = 0.04\ \mathrm{wt.\%}$. This is attributed to the dissipation of the cracks at the interface [20]. Moreover, the decrease in β with high added concentrations could be due to an increase in the weak links at the grain boundary and local structural distortions among superconducting grains [14]. By comparison of the experimental H_V values in the plateau region with the theoretical H_{PSR} calculations, it is apparent that this model is not sufficient to describe the real microhardness values of the prepared samples.

3.2.5 Modified proportional sample resistance model

When the effect of the machining-induced plastically deformed surface on the microhardness measurements was considered, the PSR model was modified and is described by the following relation:

$$F = \alpha_2 + \alpha_3 d + \alpha_4 d^2. \qquad (14)$$

The constant α_2 represents the minimum applied load for the impression length. The physical meanings of α_3 and α_4 are equivalent to those in the PSR model [16]. Fig. 8 displays a plot of the applied load versus the indentation length for $\{\mathrm{FeSiW_{11}}\}_x$(Bi,Pb)-2223 and $\{\mathrm{MnSiW_{11}}\}_x$(Bi,Pb)-2223 superconducting samples; the values obtained for the parameters (α_2, α_3 and α_4) of the MPSR model are shown in Table 3. The MPSR load-dependent microhardness (H_{MPSR}) was estimated according to the following equation (the computed values are listed in Table 2):

$$H_{\mathrm{MPSR}} = 1854.4 \times \frac{(\alpha_2 + \alpha_3 d + \alpha_4 d^2)}{d^2}. \qquad (15)$$

As seen from Table 2, H_{MPSR} decreases with an increase of $\{\mathrm{FeSiW_{11}}\}$ and $\{\mathrm{MnSiW_{11}}\}$ nanoparticle concentrations in the (Bi,Pb)-2223 superconducting phase. Additionally, the experimental H_{V} values were very similar to the true microhardness values obtained (deviation less than 4%). Hence, the MPSR model is the most reliable model to discuss the H_{V} results and mechanical properties in the plateau region of all the prepared samples in the $\{\mathrm{FeSiW_{11}}\}_x$(Bi,Pb)-2223 and $\{\mathrm{MnSiW_{11}}\}_x$(Bi,Pb)-2223 superconducting phases.

3.2.6. Indentation creep

Indentation creep experiments were performed at room temperature to study the indentation creep behaviour of $\{\mathrm{FeSiW_{11}}\}$ and $\{\mathrm{MnSiW_{11}}\}$ nanoparticle addition to the (Bi,Pb)-2223 phase. The variation of H_{V} with the dwell time (t) (10–60 s) at applied static loads of 2.94, 4.9 and 9.8 N for x = 0.00 wt.%, $\{\mathrm{FeSiW_{11}}\}_x$(Bi,Pb)-2223 with x = 0.04, 0.12 and 0.20 wt.% and $(\mathrm{MnSiW_{11}})_x$(Bi,Pb)-2223 with x = 0.08, 0.12 and 0.20 wt.% is shown in Fig. 9. As seen from Fig. 9, H_{V} decreases rapidly with the increase of t, followed by a linear decrease in the microhardness values obtained for all the samples studied for t > 40 s. Such behaviour could be considered an indication of bearing creep deformation [47]. The Sargent–Ashby model [48] was used to investigate the power-law indentation creep behaviour, where the time-dependent microhardness is described by the following relation:

$$H_{\mathrm{V}}(t) = \frac{\sigma_0}{(\eta c \sigma_0 t)^{\frac{1}{\eta}}}, \qquad (16)$$

where $H_V(t)$ is the time-dependent Vickers microhardness, σ_0 is the strain rate at reference stress r_0 and c is a constant. Fig. 10 shows plots of $\ln H_V$ versus $\ln t$ for x = 0.00 wt.%, $\{FeSiW_{11}\}_x$(Bi,Pb)-2223 with x = 0.04, 0.12 and 0.20 wt.% and $\{MnSiW_{11}\}_x$(Bi,Pb)-2223 with x = 0.08, 0.12 and 0.20 wt.% at applied static loads of 2.94, 4.9 and 9.8 N. The slope obtained from the curves is $-1/\eta$, from which the values of η were calculated and plotted as a function of the applied load in Fig. 11.

Furthermore, η values are helpful to establish the mechanisms controlling the deformation. As reported in the literature, if the values of η are around 1, then the sample suffers from a diffusion creep [49]. For η values which are close to 2, grain boundary sliding will occur within the sample [50], and for η values between 3 and 10, a dislocation creep predominates [51]. Additionally, the creation and the enhancement of new cavities depend on two important factors: the indentation caused by the applied load and the concentration of the additions. Figs. 11 and 12(a) both show that at small loads and additions there is a slight change in the η values and a decrease in the porosity values, whereas in Figs. 11 and 12(b), at high loads and with increasing concentration of $\{FeSiW_{11}\}$ and $\{MnSiW_{11}\}$, the η and porosity values increased from 6 to 10 and from 37% to 51%, respectively. This indicates the enhancement of new cavity formation. Therefore, we can conclude that the contribution of the cavities is expected to increase as the stress increases. Thus, the contribution to the creep rate as well as the stress exponent will also increase [52].

Furthermore, a correlation exists between H_V and other mechanical parameters—for example, E, Y and K. These parameters refer to the material's elastic deformation tendency under an applied force, the transition point between elastic and plastic deformation and, most importantly, from an industrial application perspective, the material's ability to resist cracks, propagation and fracture, respectively. Their values were determined for the $\{FeSiW_{11}\}_x$(Bi,Pb)-2223 and $\{MnSiW_{11}\}_x$(Bi,Pb)-2223 superconducting samples with use of Eqs. (2), (3) and (4), respectively [4, 14, 53]. The values obtained are listed in Table 4. It is known that the change in these parameters (increase or decrease) is related to the average surface energy of the sample. Thus, $\{FeSiW_{11}\}_x$(Bi,Pb)-2223 $(x \geq 0.04\ \mathrm{wt.\%})$ exhibits higher ductility and increased ability to resist cracks from indentation in comparison with $\{MnSiW_{11}\}_x$(Bi,Pb)-2223. Meanwhile, to achieve maximum enhancement in the mechanical properties of the (Bi,Pb)-2223 superconducting phase, the corresponding optimum added concentrations of $\{FeSiW_{11}\}$ and $\{MnSiW_{11}\}$ nanoparticles in both phases should not exceed 0.04 and 0.08 wt.%, respectively. According to Table 4, E, Y and K increase systematically as x increases up to 0.04 wt.% for $\{FeSiW_{11}\}_x$(Bi,Pb)-2223 and up to 0.08 wt.% for $\{MnSiW_{11}\}_x$(Bi,Pb)-2223 before showing a significant decrease with further increases in x. The main reason for these increases is the nanoparticles filling the inter-grains of the (Bi,Pb)-2223 phase [16].

4. Conclusions

The mechanical properties of the (Bi,Pb)-2223 superconducting phase with the addition of $\{FeSiW_{11}\}$ and $\{MnSiW_{11}\}$ nanoparticles were studied in detail by H_V measurements. Samples for both phases were synthesized by the solid-state reaction technique $(0.00\ \mathrm{wt.\%} \leq \mathrm{x} \leq 0.20\ \mathrm{wt.\%})$. The H_V values increased with the increase of $\{FeSiW_{11}\}$ content up to $x = 0.04\ \mathrm{wt.\%}$ and $\{MnSiW_{11}\}$ content up to $\mathrm{x} = 0.08\ \mathrm{wt.\%}$ in the (Bi,Pb)-2223 system, confirming the increase of the strength of the bonds between the grains. Thus, $\{FeSiW_{11}\}$ addition proved its superiority over $\{MnSiW_{11}\}$ addition in increasing H_V, with an increase of 173.88%. Additionally, it was determined that the addition of either $\{FeSiW_{11}\}$ or $\{MnSiW_{11}\}$ has a more significant effect than the addition of previously studied nanosized materials or nanometals. Normal ISE behaviour was observed in the measured samples because H_V decreased with increase in the applied load. For mechanical modelling of the H_V values obtained, some theoretical models (Meyer's law, HK approach, EPD model, PSR model and MPSR model) were used to understand this behaviour. The best model to describe the true microhardness values in both phases was the MPSR model. Furthermore, the mechanical parameters E, Y and K estimated from H_V values for both phases were calculated and seemed to exhibit the same trend as the H_V values as a function of nanoparticle addition.

Acknowledgements

The authors thank Beirut Arab University for research support and the National Council for Scientific Research of Lebanon for granting a doctoral fellowship to Nour El Ghouch. Additionally, the authors thank the Kamal A. Shair Central Research Science Laboratory of the Faculty of Arts and Sciences at the American University of Beirut, as well as Dr. Houssam El-Rassy, Dr. Mahmoud Khalil and Josephina Mallah for their kind and much appreciated help. Nour El Ghouch expresses her gratitude to Jamalat Al Boukhari for her valuable help, input and discussion in relation to this work.

References

[1] Y. Zalaoglu, F. Karaboga, C. Terzioglu, G. Yildirim, Improvement of mechanical performances and characteristics of bulk Bi-2212 materials exposed to Au diffusion and stabilization of durable tetragonal phase by Au, Ceram. Int. 43 (2017) 6836–6844.

[2] W. Abdeen, S. Marahba, R. Awad, A.I. Abou Aly, I.H. Ibrahim, M. Matar, Electrical and mechanical properties of (Bi,Pb)-2223 substituted by holmium, J. Adv. Ceram. 5 (2016) 54–69.

[3] S. Cavdar, E. Deniz, H. Koralay, O. Ozturk, M. Erdem, A. Gunen, The effect of PbSe addition on the mechanical properties of Bi-2212 superconductors, J. Supercond. Novel Magn. 25 (2012) 2297–2307.

[4] B. Cevizci, O. Bilgili, K. Kocabaş, The influence of Ag substitution on structural and mechanical properties of (Bi, Pb)-2223 ceramics, J. Mater. Sci. Mater. Electron. 27 (2016) 13171–13178.

[5] S. Safran, A. Kılıç, O. Ozturk, Effect of re-pelletization on structural, mechanical and superconducting properties of BSCCO superconductors, J. Mater. Sci. Mater. Electron. 28 (2017) 1799–1803.

[6] E. Asikuzun, Production procedure and characterization of Zn-doped Y-123 superconducting samples prepared by sol-gel method, J. Supercond. Novel Magn. 31 (2018) 3509–3514.

[7] R. Terzioglu, S.P. Altintas, A. Varilci, C. Terzioğlu, Modeling of micro-hardness in the Au-doped YBCO bulk superconductors, J. Supercond. Novel Magn. 32 (2019) 3377–3383.

[8] Y. Zalaoglu, E. Bekiroglu, M. Dogruer, G. Yildirim, O. Ozturk, C. Terzioglu, Comparative study on mechanical properties of undoped and Ce-doped Bi-2212 superconductors, J. Mater. Sci. Mater. Electron. 24 (2013) 2339–2345.

[9] O. Ozturk, E. Asikuzun, A.T. Tasci, T. Gokcen, H. Ada, H. Koralay, S. Cavdar, Comparison of Vickers microhardness of undoped and Ru doped BSCCO glass ceramic materials, J. Mater. Sci. Mater. Electron. 29 (2018) 3957–3966.

[10] T. Turgay, G. Yildirim, Effect of aliovalent Si/Bi partial substitution on propagation mechanisms of cracking and dislocation in Bi-2212 crystal system, J. Mater. Sci. Mater. Electron. 30 (2019) 7314–7323.

[11] K. Habanjar, F. El Haj Hassan, R. Awad, Effect of $BaFe_{12}O_{19}$ nanoparticles addition on (Bi,Pb)-2223 superconducting phase, Mod. Appl. Sci. 13 (2019) 61–71.

[12] A. Srour, W. Malaeb, M. Rekaby, R. Awad, Mechanical properties of the $(BaSnO_3)_x/Cu_{0.5}Tl_{0.5}Ba_2Ca_2Cu_3O_{10-\delta}$ superconductor phase, Phys. Scr. 92 (2017) 104002.

[13] M. Tosun, S. Ataoglu, L. Arda, O. Ozturk, E. Asikuzun, D. Akcan, O. Cakiroglu, Structural and mechanical properties of ZnMgO nanoparticles, Mater. Sci. Eng. A 590 (2014) 416–422.

[14] E. Akdemir, M. Pakdil, H. Bilge, M.F. Kahraman, E. Bekiroglu, G. Yildirim, Y. Zalaoglu, E. Doruk, M. Oz, Degeneration of mechanical characteristics and performances with Zr nanoparticles inserted in Bi-2223 superconducting matrix and increment in dislocation movement and cracks propagation, J. Mater. Sci. Mater. Electron. 27 (2016) 2276–2287.

[15] F. Kahraman, Evaluation of the Vickers microhardness and fracture toughness on hot pressed Bi-2212/Ag ceramic composites, J. Mater. Sci.: Mater. Electron. 27 (2016) 8006–8012.

[16] S. Celik, O. Ozturk, E. Coşkun, M. Sarıhan, E. Asikuzun, K. Ozturk, C. Terzioglu, Analysis of indentation size effect (ISE) behavior in low-load Vickers microhardness testing of $(Sm123)_{1-x}(Nd123)_x$ superconductor system, J. Mater. Sci. Mater. Electron. 24 (2013) 2218–2227.

[17] W. Abdeen, N.H. Mohammed, R. Awad, S.A. Mahmoud, M. Hasebbo, Influence of nano-Ag addition on the mechanical properties of $(Cu_{0.5}Tl_{0.5})$-1223 superconducting phase, J. Supercond. Novel Magn. 26 (2013) 3235–3245.

[18] M.M. Barakat, A.I. Abou-Aly, R. Awad, N.S. Aly, S. Ibrahim, Mechanical properties of $Y_{3-x}Nd_xBa_{5-x}Ca_xCu_8O_{18-\delta}$ samples, J. Alloy. Compd., 652 (2015) 158–166.

[19] R. Awad, A.I. Abou Aly, N.H. Mohammed, S. Isber, H.A. Motaweh, D. El-Said Bakeer, Investigation on superconducting properties of $GdBa_2Cu3O_{7-\delta}$ added with nanosized $ZnFe_2O_4$, J. Alloy. Compd., 610 (2014) 614–622.

[20] M. Anas, S. Ebrahim, I.G. Eldeen, R. Awad, A.I. Abou-Aly, Effect of single and multi-wall carbon nanotubes on the mechanical properties of Gd-123 superconducting phase, Chem. Phys. Lett., 686 (2017) 34–43.

[21] R. Awad, A.I. Abou Aly, M. Kamal, M. Anas, Mechanical properties of ($Cu_{0.5}Tl_{0.5}$)-1223 substituted by Pr, J. Supercond. Novel Magn. 24 (2011) 1947–1956.

[22] M.M. Barakat, Influence of $Co_{0.5}Zn_{0.5}Fe_2O_4$ nanoparticles addition on Vickers microhardness for $Cu_{0.5}Tl_{0.5}$-1223 phase, J. Supercond. Novel Magn. 30 (2017) 2945–2955.

[23] B. Özkurt, The influence of WO_3 nano-particle addition on the structural and mechanical properties of $Bi_{1.8}Sr_2Ca_{1.1}Cu_{2.1}O_y$ ceramics, J. Mater. Sci. Mater. Electron. 24 (2013) 4233–4239.

[24] F. Yahya, H. El-Rassy, G. Younes, R. Al-Oweini, Synthesis and characterisation of mesoporous hybrid silica-polyoxometalate aerogels for photocatalytic degradation of rhodamine B and methylene blue, Int. J. Environ. Anal. Chem. 99 (2019) 1375–1396.

[25] Y.-N. Gu, Y. Chen, Y.-L. Wu, S.-T. Zheng, X.-X. Li, A series of banana-shaped 3d-4f heterometallic cluster substituted polyoxometalates: syntheses, crystal structures, and magnetic properties, Inorg. Chem. 57 (2018) 2472–2479.

[26] D. Zhang, C. Zhang, P. Ma, B.S. Bassil, R. Al-Oweini, U. Kortz, J. Wang, J. Niu, Two new members of the niobium-substituted polytungstophosphate family based on hexalacunary $[H_2P_2W_{12}O_{48}]^{12-}$ building blocks, Inorg. Chem. Front. 2 (2015) 254–262.

[27] L. Youssef, G. Younes, R. Al-Oweini, Photocatalytic degradation of atrazine by heteropolyoxotungstates, J. Taibah Univ. Sci. 13 (2019) 274–279.

[28] R. Al-Oweini, B.S. Bassil, M. Itani, D.B. Emiroglu, U. Kortz, The mixed-valent 10-manganese(III/IV)-containing 36-tungsto-4-arsenate(V), $[Mn^{III}{}_6Mn^{IV}{}_4O_4(OH)_{12}(H_2O)_{12}(A\text{-}[\beta\text{-}AsW_9O_{34})_4]^{22-}$, Acta Crystallogr. Sect. C 74 (2018) 1390–1394.

[29] M. Natali, I. Bazzan, S. Goberna-Ferrón, R. Al-Oweini, M. Ibrahim, B.S. Bassil, H. Dau, F. Scandola, J.R. Galán-Mascarós, U. Kortz, A. Sartorel, I. Zaharieva, M. Bonchio, Photo-assisted water oxidation by high-nuclearity cobalt-oxo cores: tracing the catalyst fate during oxygen evolution turnover, Green Chem. 19 (2017) 2416–2426.

[30] J. Friedl, R. Al-Oweini, M. Herpich, B. Keita, U. Kortz, U. Stimming, Electrochemical studies of tri-manganese substituted Keggin polyoxoanions, Electrochim. Acta 141 (2014) 357–366.

[31] R. Al-Oweini, A. Sartorel, B.S. Bassil, M. Natali, S. Berardi, F. Scandola, U. Kortz, M. Bonchio, Photocatalytic water oxidation by a mixed-valent $Mn^{III}{}_3Mn^{IV}O_3$ manganese oxo core that mimics the natural oxygen-evolving center, Angew. Chem. Int. Ed. 53 (2014) 11182–11185.

[32] N. El Ghouch, R. Al-Oweini, R. Awad, Synthesis, characterization and electrical properties of hybrid mono-iron-substituted undecatungstosilicate/(Bi,Pb)-2223 phase superconductors, Mater. Res. Express 6 (2019) 116001.

[33] N. El Ghouch, R. Al-Oweini, R. Awad, Preparation and physical properties of $(Bi_{1.8}Pb_{0.4})Sr_2Ca_2Cu_3O_{10+\delta}$ superconductors impregnated with mangano(II)undecatungstosilicate nanomaterials, Appl. Phys. A 125 (2019) 854.

[34] N.E. Ghouch, R. Al-Oweini, R. Awad, Effects of adding transition metal-substituted polyoxotungstates on the frequency and temperature-dependent dielectric properties of $(Bi_{1.8}Pb_{0.4})Sr_2Ca_2Cu_3O_{10+\delta}$ superconducting phase, J. Low Temp. Phys. 200 (2020) 62–75.

[35] A.P. Ginsberg (Ed.), Inorganic Syntheses, Vol. 27, John Wiley & Sons, Toronto, 1990.

[36] M.J. Ekundayo, R. Rezaee, Volumetric measurements of methane-coal adsorption and desorption isotherms—effects of equations of state and implication for initial gas reserves, Energies 12 (2019) 2022.

[37] S. Venkateswarlu, M. Yoon, Rapid removal of cadmium ions using green-synthesized Fe_3O4 nanoparticles capped with diethyl-4-(4 amino-5-mercapto-4 H-1, 2, 4-triazol-3-yl) phenyl phosphonate, RSC Adv. 5 (2015) 65444–65453.

[38] S. Brunauer, P.H. Emmett, E. Teller, Adsorption of gases in multimolecular layers, J. Am. Chem. Soc. 60 (1938) 309–319.

[39] E.P. Barrett, L.G. Joyner, P.P. Halenda, The determination of pore volume and area distributions in porous substances. I. Computations from nitrogen isotherms, J. Am. Chem. Soc., 73 (1951) 373–380.

[40] L. Han, S. Xue, S. Zhao, J. Yan, L. Qian, M. Chen, Biochar supported nanoscale iron particles for the efficient removal of methyl orange dye in aqueous solutions, PLoS One 10 (2015) e0132067.

[41] C.E. Foerster, E. Lima, P. Rodrigues Jr., F.C. Serbena, C.M. Lepienski, M.P. Cantão, A.R. Jurelo, X. Obradors, Mechanical properties of Ag-doped top-seeded melt-grown YBCO pellets, Braz. J. Phys. 38 (2008) 341–345.

[42] B. Sahoo, D. Behera, Investigation of superconducting and elastic parameters of YBCO/LSMO thick films, J. Mater. Sci. Mater. Electron. 30 (2019) 12992–13004.

[43] C. Hays, E.G. Kendall, An analysis of Knoop microhardness, Metallography 6 (1973) 275–282.

[44] A. Leenders, M. Mich, H.C. Freyhard, Influence of thermal cycling on the mechanical properties of VGF melt-textured YBCO, Physica C Supercond. 279 (1997) 173–180.

[45] Z. Li, A. Ghosh, A.S. Kobayashi, R.C. Bradt, Indentation fracture toughness of sintered silicon carbide in the Palmqvist crack regime, J. Am. Ceram. Soc. 72 (1989) 904–911.

[46] H. Li, R.C. Bradt, The microhardness indentation load/size effect in rutile and cassiterite single crystals, J. Mater. Sci. 28 (1993) 917–926.

[47] H.M. Zaki, A.M. Abdel-Daiem, Y.I. Swilem, F. El-Tantawy, F.M. Al-Marzouki, A.A. Al-Ghamdi, S. Al-Heniti, F.S. Al-Hazmi, T.S. Al-Harbi, Indentation creep behavior and microstructure of Cu-Ge ferrites, Mater. Sci. Appl. 2 (2011) 1076–1082.

[48] P.M. Sargent, M.F. Ashby, Indentation creep, Mater. Sci. Technol. 8 (1992) 594–601.

[49] T.G. Langdon, Identifiying creep mechanisms at low stresses, Mater. Sci. Eng. A, 283 (2000) 266–273.

[50] B. Walser, O.D. Sherby, The structure dependence of power law creep, Scr. Metall. 16 (1982) 213–219.

[51] C. Goetze, W.F. Brace, Laboratory observations of high-temperature rheology of rocks, Tectonophysics 13 (1972) 583–600.

[52] M. Kašiarová, B. Shollock, A. Boccaccini, J. Dusza, Microstructure and creep behavior of a Si_3N_4–SiC micronanocomposite, J. Amm Ceram. Soc. 92 (2009) 439–444.

[53] H. Koralay, A. Arslan, S. Cavdar, O. Ozturk, E. Asikuzun, A. Gunen, A.T. Tasci, Structural and mechanical characterization of $Bi_{1.75}Pb_{0.25}Sr_2Ca_2Cu_{3-x}Sn_xO_{10+y}$ superconductor ceramics using Vickers microhardness test, J. Mater. Sci. Mater. Electron. 24 (2013) 4270–4278.

Fig. 1. Typical nitrogen adsorption–desorption isotherms for (a) x = 0.00 wt.%, (b) x = 0.04 wt.% {$FeSiW_{11}$}, (c) x = 0.08 wt.% {$FeSiW_{11}$} and (d) x= 0.12 wt.% {$MnSiW_{11}$} superconducting samples.

Fig. 2. Pore size distribution for (a) x = 0.00 wt%, (b) x= 0.04 wt% {$FeSiW_{11}$}, (c) x= 0.08 wt.% {$FeSiW_{11}$} and (d) x= 0.12 wt.% {$MnSiW_{11}$} superconducting samples.

Fig. 3. H_V as a function of the applied static load F for the $\{FeSiW_{11}\}_x$(Bi,Pb)-2223 and $\{MnSiW_{11}\}_x$(Bi,Pb)-2223 phases at a dwell time of 30 s. The inset shows the indentation at $F = 0.245$ N for $x = 0.12$ wt.%.

Fig. 4. ln F versus ln d for the $\{FeSiW_{11}\}_x$(Bi,Pb)-2223 and $\{MnSiW_{11}\}_x$(Bi,Pb)-2223 phases at a dwell time of 30 s.

Fig. 5. Effective load F as a function of d^2 for the $\{FeSiW_{11}\}_x$(Bi,Pb)-2223 and $\{MnSiW_{11}\}_x$(Bi,Pb)-2223 phases at a dwell time of 30 s.

Fig. 6. Linear plot of $F^{0.5}$ versus d for the $\{FeSiW_{11}\}_x$(Bi,Pb)-2223 and $\{MnSiW_{11}\}_x$(Bi,Pb)-2223 phases at a dwell time of 30 s.

Fig. 7. F/d versus d for $\{FeSiW_{11}\}_x$(Bi,Pb)-2223 and $\{MnSiW_{11}\}_x$(Bi,Pb)-2223 at a dwell time of 30 s.

Fig. 8. F versus d for $\{FeSiW_{11}\}_x$(Bi,Pb)-2223 and $\{MnSiW_{11}\}_x$(Bi,Pb)-2223 at a dwell time of 30 s.

Fig. 9. Variation of H_V with time at applied static loads of (a) 2.94 N, (b) 4.9 N and (c) 9.8 N for the $\{FeSiW_{11}\}_x$(Bi,Pb)-2223 and $\{MnSiW_{11}\}_x$(Bi,Pb)-2223 phases.

Fig. 10. Variation of ln H_V with ln t at applied static loads of (a) 2.94 N, (b) 4.9 N and (c) 9.8 N for the $\{FeSiW_{11}\}_x$(Bi,Pb)-2223 and $\{MnSiW_{11}\}_x$(Bi,Pb)-2223 phases.

Fig. 11. Stress exponent η versus applied static load F for $\{FeSiW_{11}\}_x$(Bi,Pb)-2223 and $\{MnSiW_{11}\}_x$(Bi,Pb)-2223 superconducting samples at (a) lower and (b) higher concentrations.

Fig. 12. Relationship between the porosity and the stress exponent and x (wt.%) for (a) $\{FeSiW_{11}\}_x$(Bi,Pb)-2223 and (b) $\{MnSiW_{11}\}_x$(Bi,Pb)-2223 superconducting samples.

Table 1. Brunauer–Emmett–Teller surface analysis data for the $\{FeSiW_{11}\}_x$(Bi,Pb)-2223 and $\{MnSiW_{11}\}_x$(Bi,Pb)-2223 phases.

x (wt.%)	Specific surface area (m^2/g)	Total pore volume (cm^3/g)
0.00	0.56	0.030
$\{FeSiW_{11}\}$		
0.04	14.48	0.043
0.08	9.69	0.037

$\{MnSiW_{11}\}$		
0.12	0.42	0.001

Table 2. Fitting parameters obtained from the theoretical models for the $\{FeSiW_{11}\}_x$(Bi,Pb)-2223 and $\{MnSiW_{11}\}_x$(Bi,Pb)-2223 phases with 0.00 wt. % $\leq x \leq$ 0.20 wt. %.

x (wt.%)	Fitting relations	H_V	H_{HKind}	H_{EPDind}	H_{PSRind}	H_{MPSR}
		(GPa)	(GPa)	(GPa)	(GPa)	(GPa)
0.00	$y = 0.0073x^2 - 0.1086x + 0.6053$	0.268	0.222	0.198	0.186	0.258
$\{FeSiW_{11}\}$						
0.02	$y = 0.0239x^2 - 0.3339x + 1.6534$	0.699	0.619	0.544	0.510	0.684
0.04	$y = 0.0332x^2 - 0.4617x + 2.0517$	0.734	0.613	0.526	0.475	0.703
0.08	$y = 0.0143x^2 - 0.2123x + 1.3394$	0.670	0.595	0.534	0.512	0.657
0.12	$y = 0.0155x^2 - 0.2228x + 1.2962$	0.625	0.558	0.496	0.473	0.610
0.16	$y = 0.0135x^2 - 0.1994x + 1.2043$	0.584	0.509	0.456	0.435	0.574
0.20	$y = 0.0130x^2 - 0.1889x + 1.1417$	0.561	0.500	0.446	0.426	0.551
$\{MnSiW_{11}\}$						
0.02	$y = 0.0233x^2 - 0.3310x + 1.5032$	0.534	0.446	0.386	0.349	0.521
0.04	$y = 0.0269x^2 - 0.3740x + 1.5284$	0.462	0.391	0.330	0.288	0.454
0.08	$y = 0.0153x^2 - 0.2181x + 1.1910$	0.545	0.478	0.425	0.402	0.531
0.12	$y = 0.0142x^2 - 0.2022x + 1.1243$	0.523	0.469	0.416	0.395	0.515
0.16	$y = 0.0072x^2 - 0.1032x + 0.7901$	0.477	0.441	0.406	0.397	0.469
0.20	$y = 0.0081x^2 - 0.1177x + 0.7361$	0.376	0.335	0.301	0.289	0.368

Table 3. Fitting relationship for H_V values with regard to the applied test load; experimental and theoretical microhardness analysis results for the $\{FeSiW_{11}\}_x$(Bi,Pb)-2223 and $\{MnSiW_{11}\}_x$(Bi,Pb)-2223 phases with 0.00 wt. % $\leq x \leq$ 0.20 wt. %.

x	Meyer	HK	EPD	PSR	MPSR

	n	$A \times 10^{-3}$	W	$A_1 \times 10^{-4}$	$A_2 \times 10^{-3}$	d_0	$\alpha \times 10^{-3}$	$\beta \times 10^{-4}$	α_2	$\alpha_3 \times 10^{-2}$	$\alpha_4 \times 10^{-4}$
(wt.%)		(N/μm^2)	(N)	(N/μm^2)	(N/μm^2)	(μm)	(N/μm)	(N/μm^2)	(N)	(N/μm)	(N/μm^2)
0.00 {FeSiW$_{11}$}	1.570	1.427	0.59	1.20	0.10	30.30	8.53	1.01	−0.36	1.78	0.65
0.02	1.556	3.212	0.48	3.34	0.29	16.69	12.9	2.75	−0.14	1.91	2.35
0.04	1.487	4.666	0.60	3.31	0.28	20.79	16.6	2.56	−0.17	2.49	2.01
0.08	1.633	2.175	0.46	3.21	0.28	15.35	11.1	2.76	−0.22	2.04	2.18
0.12	1.613	2.253	0.44	3.01	0.26	15.98	10.8	2.56	−0.13	1.66	2.20
0.16	1.616	2.105	0.49	2.75	0.24	17.42	10.9	2.35	−0.25	2.07	1.79
0.20	1.624	1.967	0.45	2.70	0.24	16.87	10.2	2.30	−0.17	1.70	1.92
{MnSiW$_{11}$}	1.489	3.693	0.63	2.41	0.20	24.55	14.34	1.89	−0.24	2.42	1.34
0.02	1.436	4.377	0.65	2.11	0.17	28.65	15.03	1.56	−0.14	2.12	1.22
0.04	1.590	2.255	0.48	2.58	0.22	18.30	10.85	2.17	−0.18	1.79	1.77
0.08	1.602	2.065	0.44	2.53	0.22	17.84	10.27	2.13	−0.12	1.53	1.85
0.12	1.720	1.050	0.30	2.38	0.21	12.55	6.48	2.14	−0.10	1.00	1.96
0.16	1.640	1.302	0.43	1.81	0.16	19.48	7.91	1.56	−0.19	1.39	1.29
0.20											

EPD, elastic–plastic deformation; HK, Hays–Kendall; MPSR, modified proportional sample resistance; PSR, proportional sample resistance.

Table 4. Mechanical parameters E, Y and K for the $\{FeSiW_{11}\}_x$(Bi,Pb)-2223 and $\{MnSiW_{11}\}_x$(Bi,Pb)-2223 phases.

x (wt.%)	E (GPa)	Y (GPa)	K (GPa μm$^{1/2}$)
0.00 {FeSiW$_{11}$}	21.96	0.089	0.612

0.04	60.23	0.244	1.414
0.12	51.24	0.208	1.056
0.20	45.99	0.187	0.972
{MnSiW$_{11}$}			
0.08	44.68	0.181	0.984
0.12	42.90	0.174	0.938
0.20	30.83	0.125	0.698

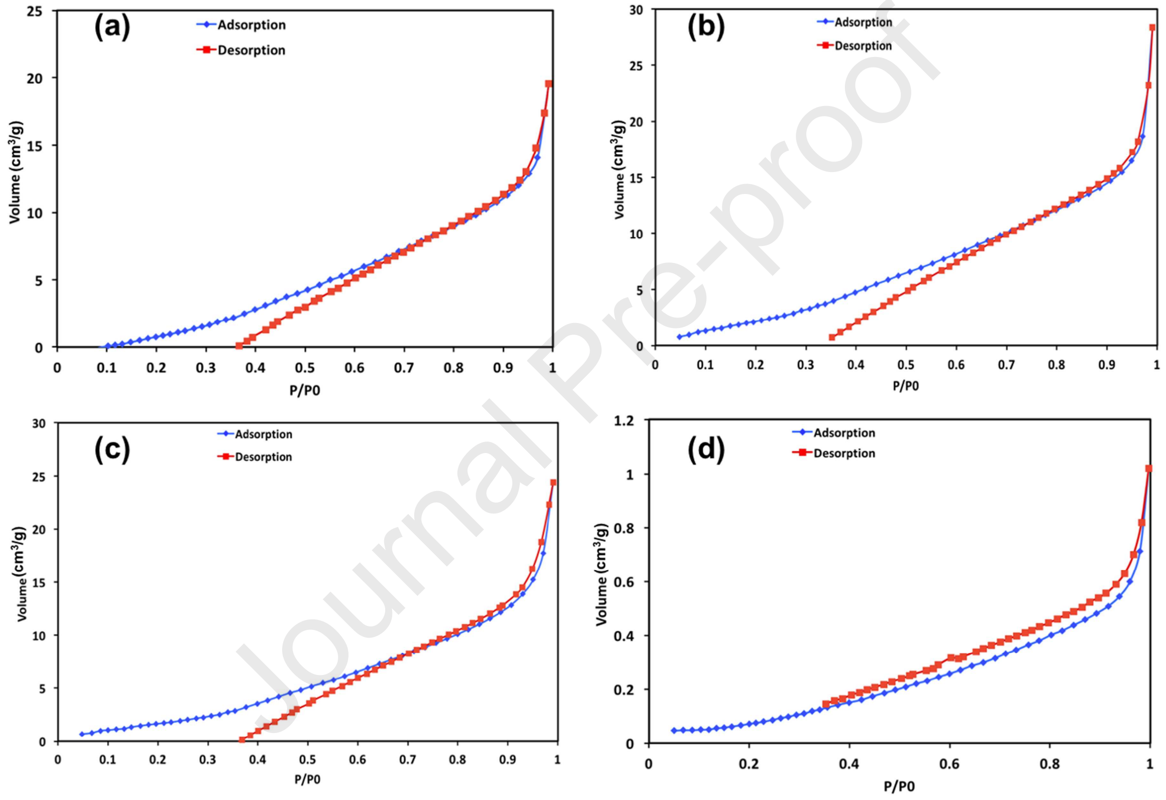

Fig. 1

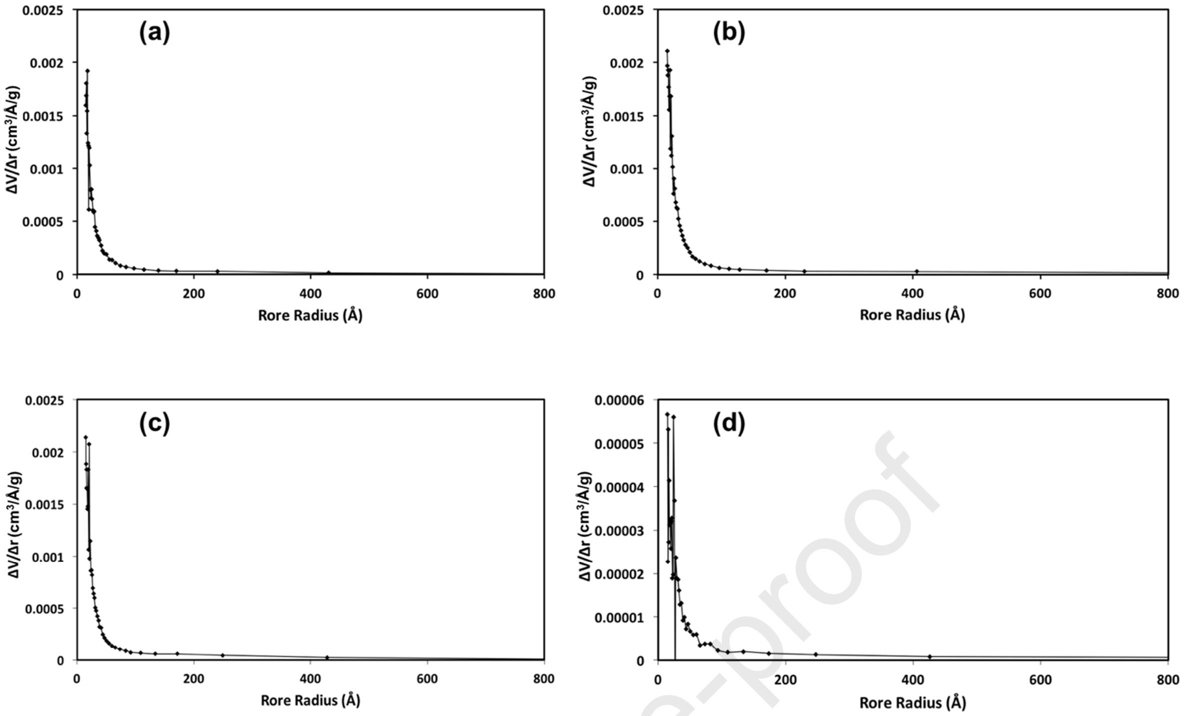
(a)
(b)
(c)
(d)
ΔV/Δr (cm³/A/g)
Rore Radius (Å)
0
0.0005
0.001
0.0015
0.002
0.0025
0.00001
0.00002
0.00003
0.00004
0.00005
0.00006
200
400
600
800

Fig. 2

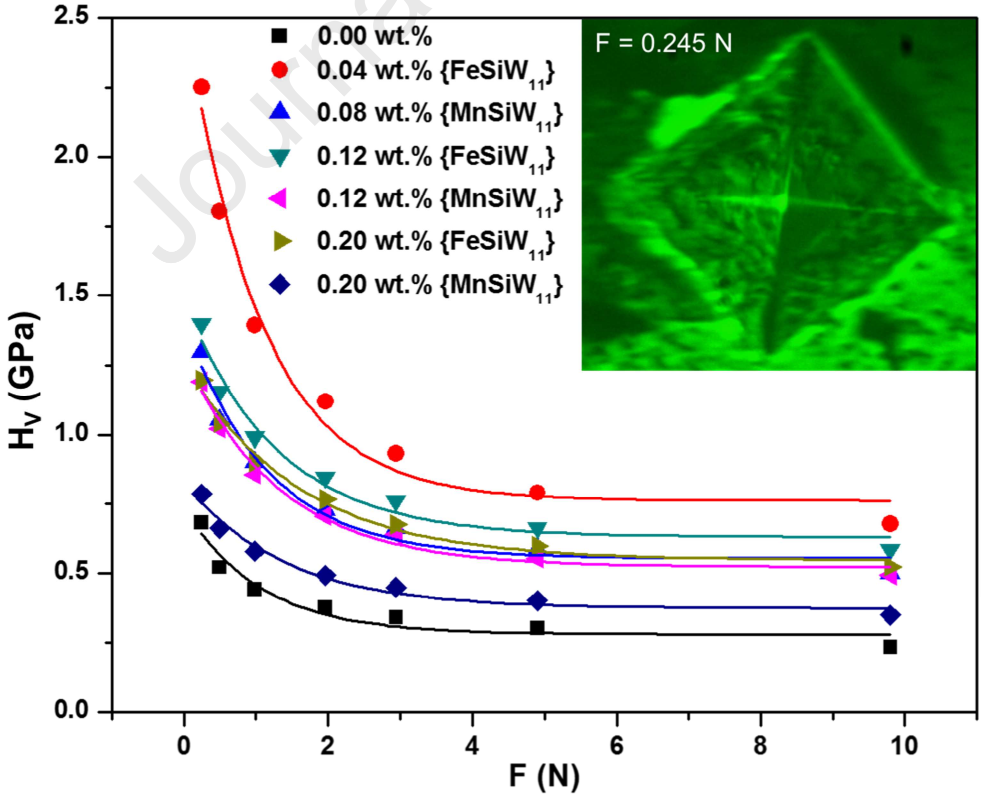
F = 0.245 N
0.00 wt.%
0.04 wt.% {FeSiW11}
0.08 wt.% {MnSiW11}
0.12 wt.% {FeSiW11}
0.12 wt.% {MnSiW11}
0.20 wt.% {FeSiW11}
0.20 wt.% {MnSiW11}
HV (GPa)
F (N)
0.0
0.5
1.0
1.5
2.0
2.5
0
2
4
6
8
10

Fig. 3

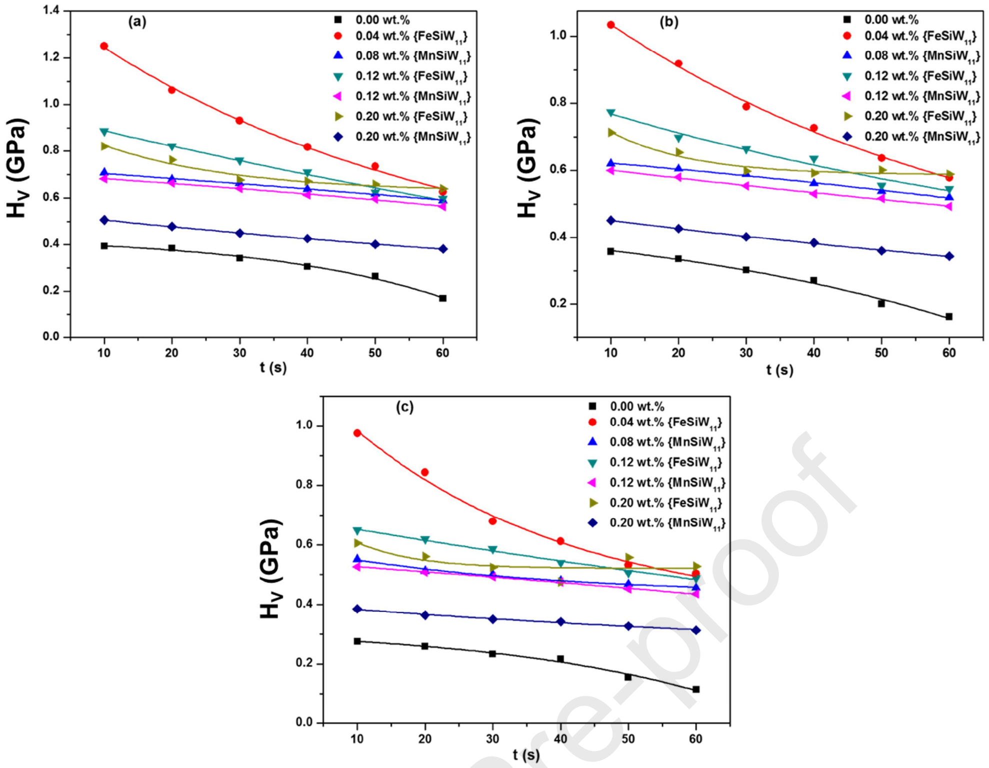
(a)
(b)
(c)
H_V (GPa)
t (s)
0.00 wt.%
0.04 wt.% {$FeSiW_{11}$}
0.08 wt.% {$MnSiW_{11}$}
0.12 wt.% {$FeSiW_{11}$}
0.12 wt.% {$MnSiW_{11}$}
0.20 wt.% {$FeSiW_{11}$}
0.20 wt.% {$MnSiW_{11}$}
0.0
0.2
0.4
0.6
0.8
1.0
1.2
1.4
10
20
30
40
50
60

Fig. 9

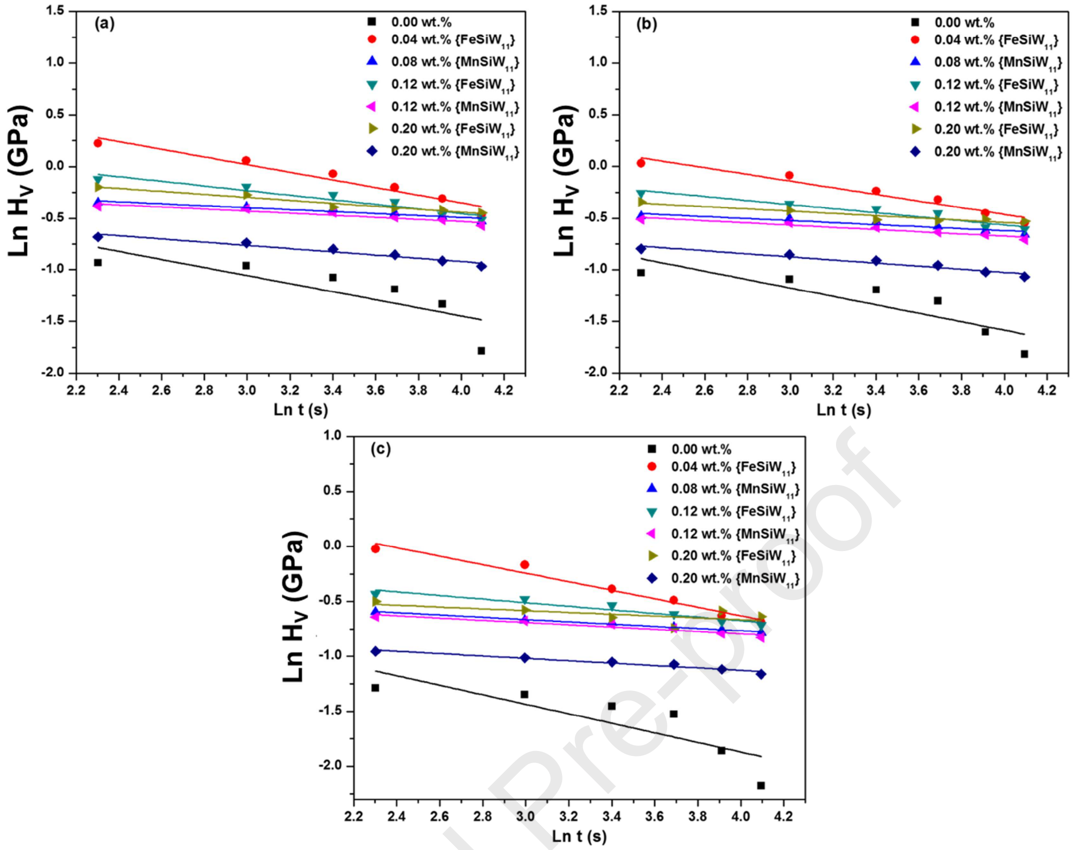
(a)
(b)
(c)
0.00 wt.%
0.04 wt.% {FeSiW$_{11}$}
0.08 wt.% {MnSiW$_{11}$}
0.12 wt.% {FeSiW$_{11}$}
0.12 wt.% {MnSiW$_{11}$}
0.20 wt.% {FeSiW$_{11}$}
0.20 wt.% {MnSiW$_{11}$}
Ln H$_V$ (GPa)
Ln t (s)
1.5
1.0
0.5
0.0
-0.5
-1.0
-1.5
-2.0
2.2
2.4
2.6
2.8
3.0
3.2
3.4
3.6
3.8
4.0
4.2

Fig. 10

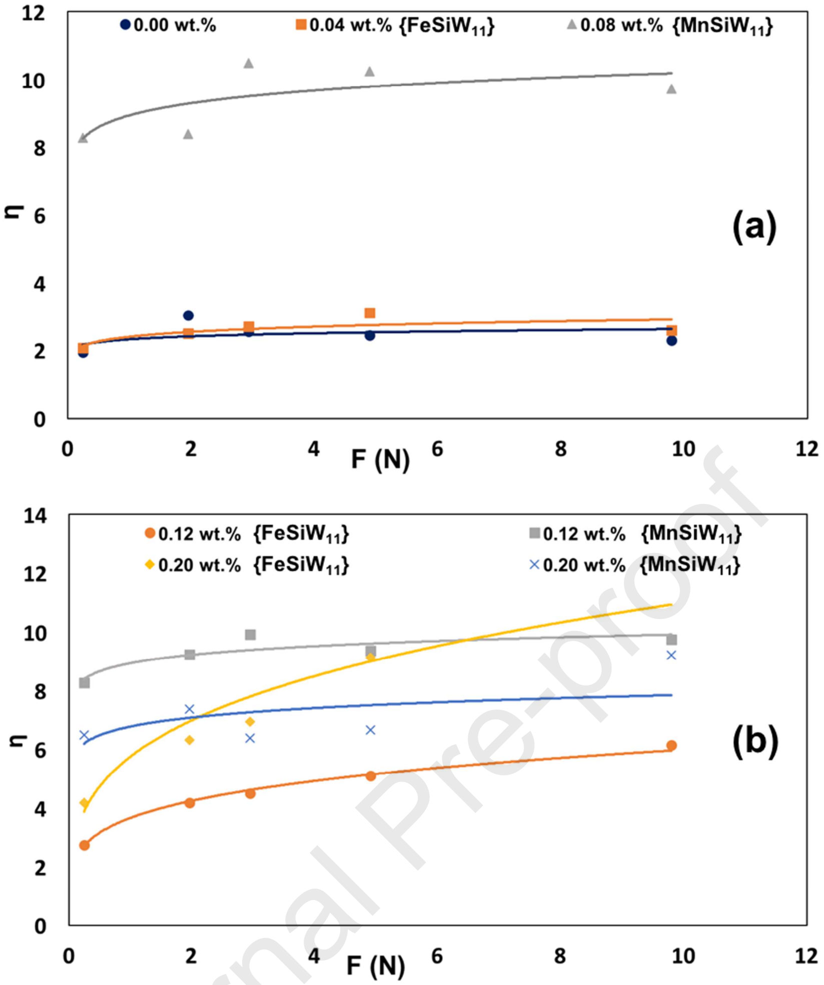
0.00 wt.%
0.04 wt.% {FeSiW11}
0.08 wt.% {MnSiW11}
(a)
η
F (N)
0
2
4
6
8
10
12
0.12 wt.% {FeSiW11}
0.20 wt.% {FeSiW11}
0.12 wt.% {MnSiW11}
0.20 wt.% {MnSiW11}
(b)
14

Fig. 11

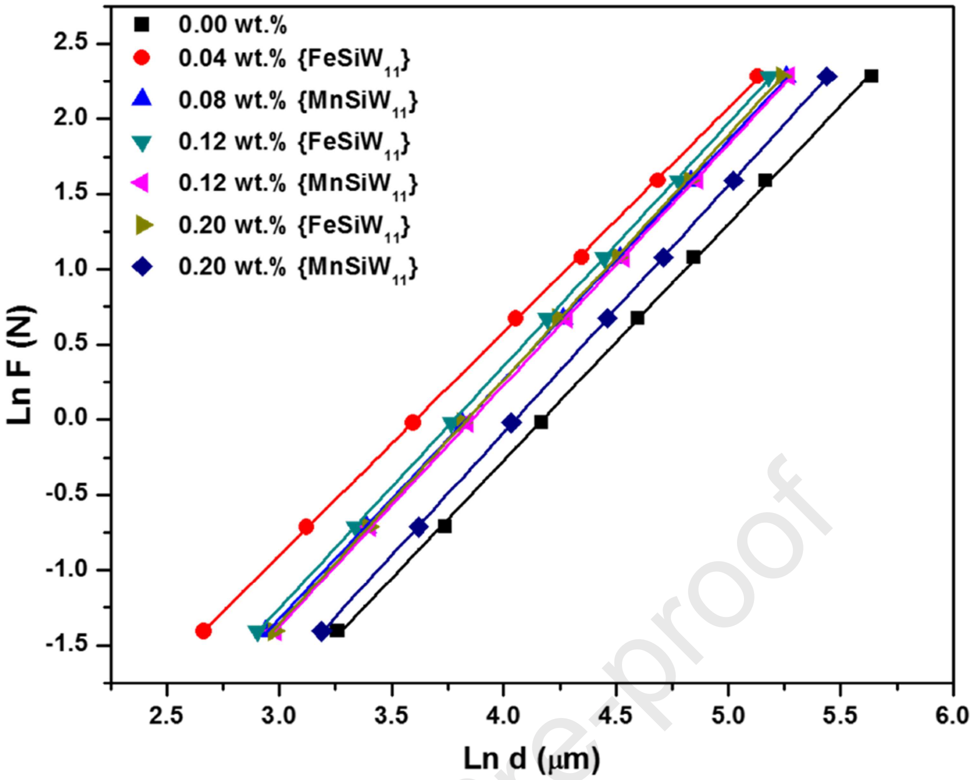
■ 0.00 wt.%
● 0.04 wt.% {$FeSiW_{11}$}
▲ 0.08 wt.% {$MnSiW_{11}$}
▼ 0.12 wt.% {$FeSiW_{11}$}
◄ 0.12 wt.% {$MnSiW_{11}$}
► 0.20 wt.% {$FeSiW_{11}$}
◆ 0.20 wt.% {$MnSiW_{11}$}
Ln F (N)
2.5
2.0
1.5
1.0
0.5
0.0
-0.5
-1.0
-1.5
2.5
3.0
3.5
4.0
4.5
5.0
5.5
6.0
Ln d (μm)

Fig. 4

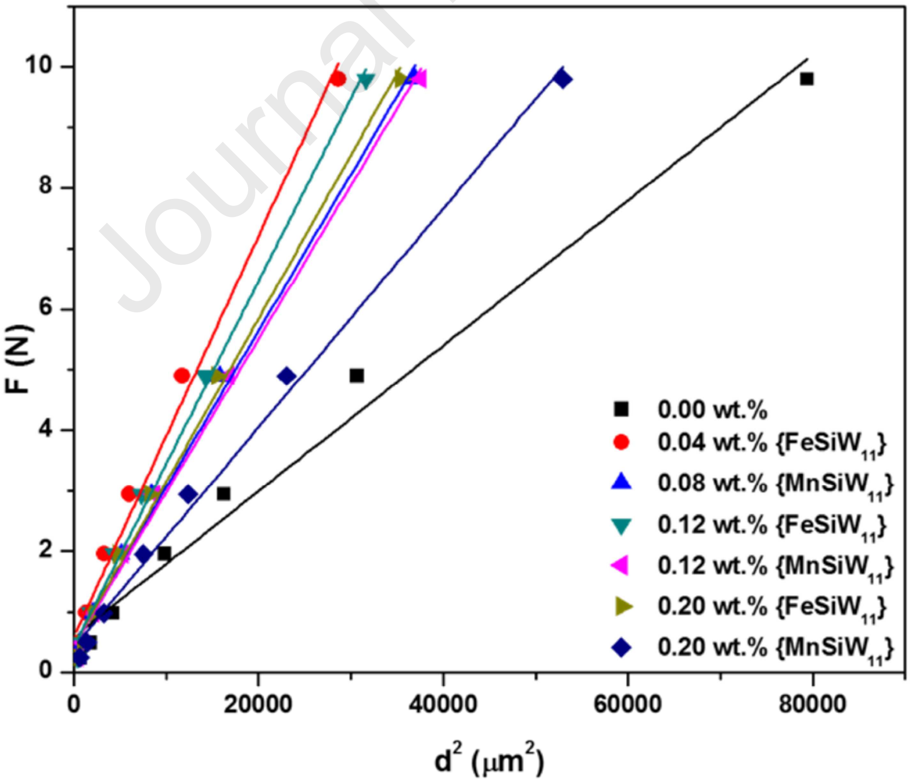
F (N)
10
8
6
4
2
0
0
20000
40000
60000
80000
d^2 (μm^2)
■ 0.00 wt.%
● 0.04 wt.% {$FeSiW_{11}$}
▲ 0.08 wt.% {$MnSiW_{11}$}
▼ 0.12 wt.% {$FeSiW_{11}$}
◄ 0.12 wt.% {$MnSiW_{11}$}
► 0.20 wt.% {$FeSiW_{11}$}
◆ 0.20 wt.% {$MnSiW_{11}$}

Fig. 5

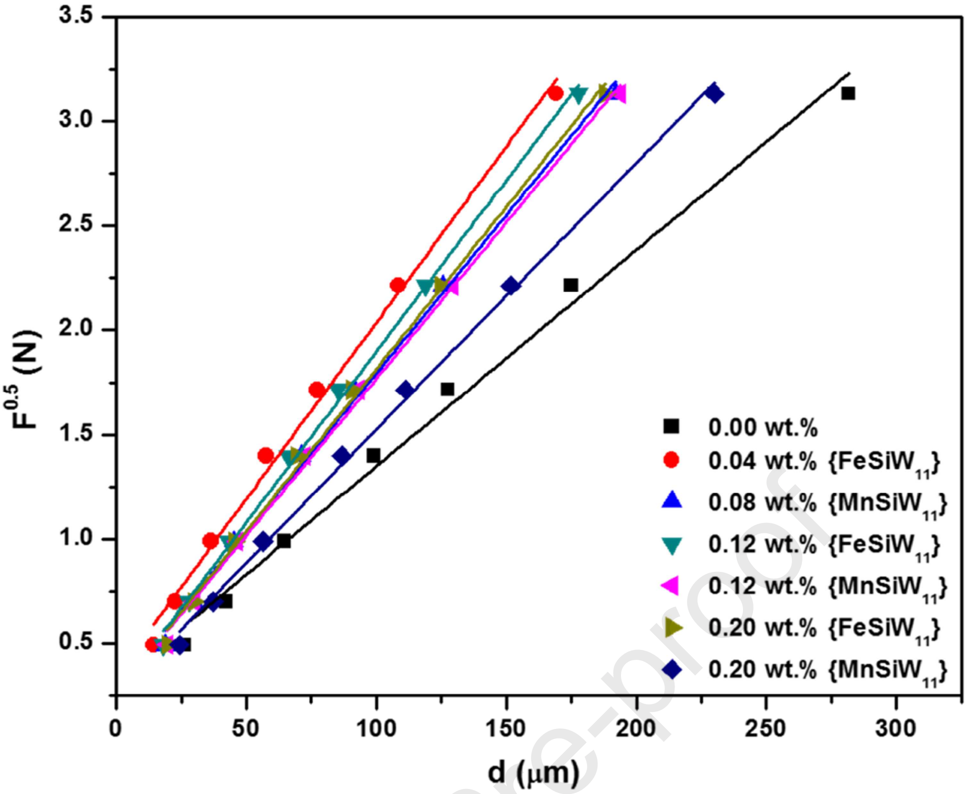
3.5
3.0
2.5
2.0
1.5
1.0
0.5
$F^{0.5}$ (N)
0
50
100
150
200
250
300
d (μm)
0.00 wt.%
0.04 wt.% {FeSiW$_{11}$}
0.08 wt.% {MnSiW$_{11}$}
0.12 wt.% {FeSiW$_{11}$}
0.12 wt.% {MnSiW$_{11}$}
0.20 wt.% {FeSiW$_{11}$}
0.20 wt.% {MnSiW$_{11}$}

Fig. 6

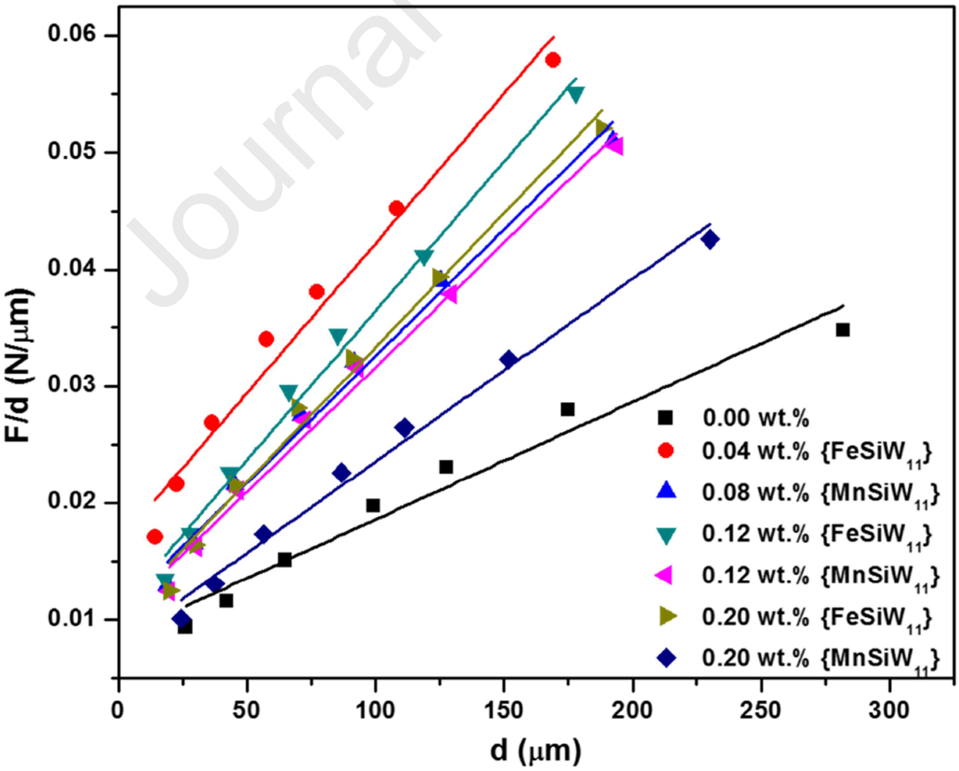
0.06
0.05
0.04
0.03
0.02
0.01
F/d (N/μm)
0
50
100
150
200
250
300
d (μm)
0.00 wt.%
0.04 wt.% {FeSiW$_{11}$}
0.08 wt.% {MnSiW$_{11}$}
0.12 wt.% {FeSiW$_{11}$}
0.12 wt.% {MnSiW$_{11}$}
0.20 wt.% {FeSiW$_{11}$}
0.20 wt.% {MnSiW$_{11}$}

Fig. 7

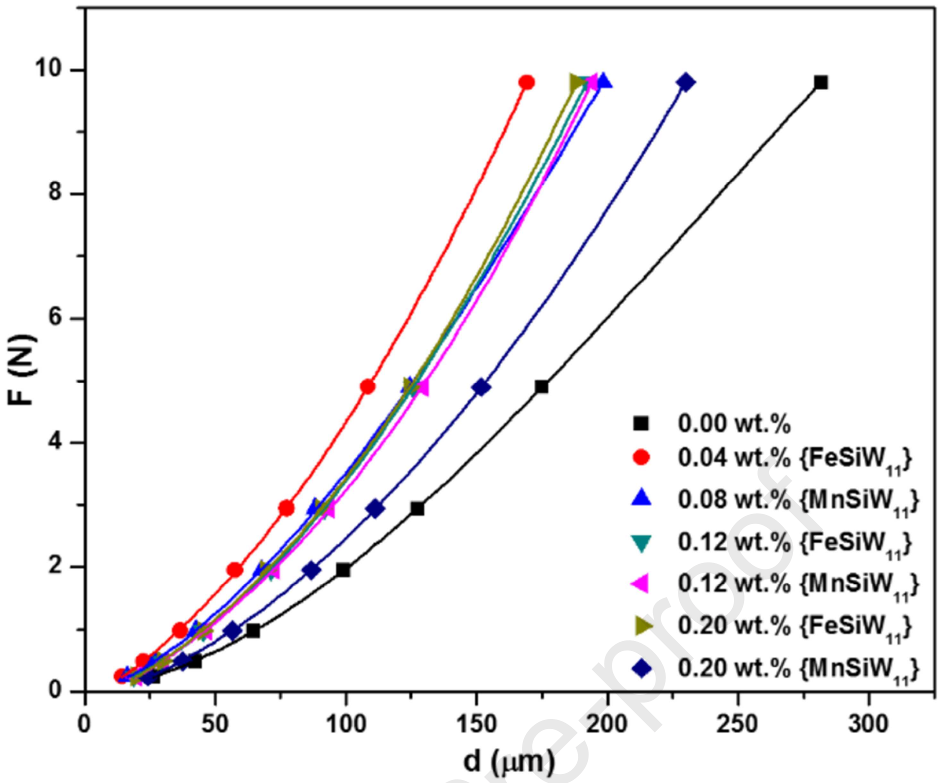
F (N)
0
2
4
6
8
10
0
50
100
150
200
250
300
d (µm)
0.00 wt.%
0.04 wt.% {FeSiW$_{11}$}
0.08 wt.% {MnSiW$_{11}$}
0.12 wt.% {FeSiW$_{11}$}
0.12 wt.% {MnSiW$_{11}$}
0.20 wt.% {FeSiW$_{11}$}
0.20 wt.% {MnSiW$_{11}$}

Fig. 8

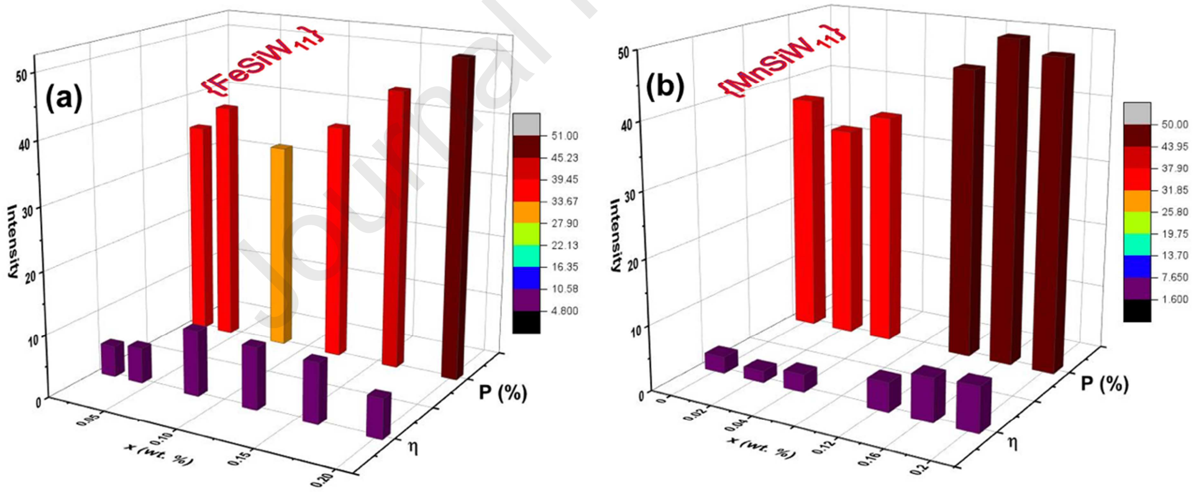
(a)
{FeSiW$_{11}$}
Intensity
0
10
20
30
40
50
0.05
0.10
0.15
0.20
x (wt. %)
P (%)
η
51.00
45.23
39.45
33.67
27.90
22.13
16.35
10.58
4.800
(b)
{MnSiW$_{11}$}
Intensity
0
10
20
30
40
50
0
0.02
0.04
0.12
0.16
0.2
x (wt. %)
P (%)
η
50.00
43.95
37.90
31.85
25.80
19.75
13.70
7.650
1.600

Fig. 12

Fig. 4. ln F versus ln d for the $\{FeSiW_{11}\}_x$(Bi,Pb)-2223 and $\{MnSiW_{11}\}_x$(Bi,Pb)-2223 phases at a dwell time of 30 s.

Fig. 5. Effective load F as a function of d^2 for the $\{FeSiW_{11}\}_x$(Bi,Pb)-2223 and $\{MnSiW_{11}\}_x$(Bi,Pb)-2223 phases at a dwell time of 30 s.

Fig. 6. Linear plot of $F^{0.5}$ versus d for the $\{FeSiW_{11}\}_x$(Bi,Pb)-2223 and $\{MnSiW_{11}\}_x$(Bi,Pb)-2223 phases at a dwell time of 30 s.

Fig. 7. F/d versus d for $\{FeSiW_{11}\}_x$(Bi,Pb)-2223 and $\{MnSiW_{11}\}_x$(Bi,Pb)-2223 at a dwell time of 30 s.

Fig. 8. F versus d for $\{FeSiW_{11}\}_x$(Bi,Pb)-2223 and $\{MnSiW_{11}\}_x$(Bi,Pb)-2223 at a dwell time of 30 s.

Fig. 12. Relationship between the porosity and the stress exponent and x (wt.%) for (a) $\{FeSiW_{11}\}_x$(Bi,Pb)-2223 and (b) $\{MnSiW_{11}\}_x$(Bi,Pb)-2223 superconducting samples.

Comparative study on the effect of adding two transition-metal-substituted polyoxometalates on the mechanical properties of the (Bi,Pb)-2223 superconducting phase

Highlights

- The Vickers microhardness of new polyoxometalate–(Bi,Pb)-2223 composites was studied.
- The Vickers microhardness was increased by addition of both polyoxometalates.
- All measured samples exhibit normal indentation size effect behaviour.
- The experimental data are well fitted by the modified proportional sample resistance model.
- Enhancement of new cavity formation was implied from indentation creep analysis.

Declaration of interests

☒ The authors declare that they have no known competing financial interests or personal relationships that could have appeared to influence the work reported in this paper.

☐The authors declare the following financial interests/personal relationships which may be considered as potential competing interests: